J Mater Sci (2009) 44:5393–5407
DOI 10.1007/s10853-009-3567-8

FERROELECTRICS

Factors affecting the performance of piezoelectric bending actuators for advanced applications: an overview

Tao Li · Y. H. Chen · J. Ma

Received: 11 March 2009 / Accepted: 12 May 2009 / Published online: 27 May 2009

Abstract The behaviors of piezoelectric bending actuators both in static and dynamic conditions driven by a high electric field were investigated and are summarized in this paper. In the static condition, the polarization and the displacement were measured and analyzed. It was found that the displacement hysteresis loop is the superposition of displacement loop induced by each layer of the actuator. The shape variation of the hysteresis loop is affected by the actuator configuration, i.e., the arrangement of electric field and poling direction. When the poling direction is parallel to an even electric field, such as parallel bimorph, the domain turns to switch at the exact coercive field of the piezoelectric material. However, when the poling direction is antiparallel to the electric field, such as series bimorph, the effect of electric field redistribution will take place during the domain reorientation, which reduces the actual electric field in the electric field–poling direction antiparallel layer, therefore prohibiting further domain reorientation. As a result, the series bimorph is noted to be more resistant to domain reorientation than the parallel bimorph. In the dynamic condition, the functions and relations of vibration velocity, heat generation, stress, and frequency were examined both theoretically and experimentally. It was found that the stress effect dominates at low frequency. At low frequency the failure mode of the actuator is often the physical fracture of the material. However, at high frequency, the failure modes mainly resulted from heat generation, unstable operation, depoling, and domain reorientation of the actuators. The vibration velocity will also decrease accordingly at the high frequency range due to more losses and heat generation.

T. Li · Y. H. Chen · J. Ma (✉)
School of Materials Science and Engineering, Nanyang Technological University, Singapore 639798, Singapore
e-mail: asjma@ntu.edu.sg

Introduction

The applications of piezoelectric actuators have been universal and numerous in many areas due to their advantages of good displacement resolution, good mechanical durability, high speed, large output force, low power consumption, and wide frequency band [1–13]. There are generally two types of widely applied piezoelectric actuators, namely, bending and multilayer actuator [7]. Compared with the multilayer actuator, the bending actuator usually produces a lower blocking force. However, its displacement is proportional to the square of the length, which makes it an effective device and a good candidate for many large displacement applications, such as the driver of an impedance pump [7, 14, 15]. The common configurations of bending actuators consist of bimorph, unimorph, monomorph, and tube as shown in Fig. 1 [1–13, 16–19]. The bimorph actuator is usually fabricated by bonding two piezoelectric plates, and driven by the opposite electric fields. In series bimorph (Fig. 1a), the upper and lower layer piezoelectric plates have antiparallel poling direction and the electric field is applied across the total thickness of the actuator. In the parallel bimorph (Fig. 1b), the upper and lower layer plates are poled in parallel direction, and electric fields with the same magnitude and opposite polarity are applied to the individual plate. The unimorph actuator (Fig. 1c) is usually fabricated by bonding the piezoelectric plate to an elastic sheet. The piezoelectric plate is poled and driven by the electric field

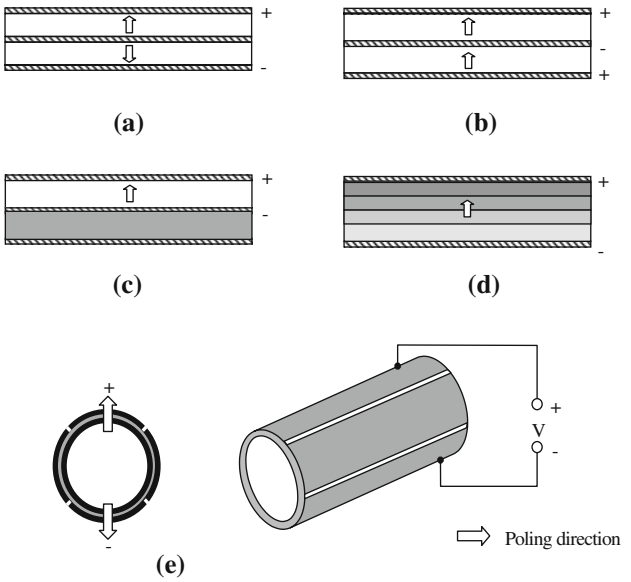

Fig. 1 Configurations of the piezoelectric bending actuators. **a** Series bimorph. The upper and lower layers have antiparallel poling direction. The electric field is across the total thickness. **b** Parallel bimorph. The upper and lower layers have parallel poling direction. The electric field is applied in each layer. **c** Unimorph. Poled piezoelectric plate is bonded to an elastic sheet. The electric field is applied to the piezoelectric layer. **d** Monomorph. It is a monolithic plate with gradient piezoelectric properties. It is poled in thickness direction and electric field is applied across the total thickness. **e** Piezo tube. It is poled in radial direction and electric field is applied across one pair of the opposing electrodes

in the thickness direction. Monomorph (Fig. 1d), on the other hand, is just a monolithic ceramic plate. In this paper, the technique of electrophoretic deposition (EPD) was applied to fabricate the monomorph actuator [20–23]. Over the cross section of the actuator, the piezoelectric properties were made to vary in a graded manner (functional graded materials (FGM) structure). The actuator is poled in the thickness direction with the electric field applied between the top and bottom electrodes. Lastly, the piezoelectric tubular actuator (Fig. 1e) is a hollow tube, and poled in the radial direction. The electrode in the outer surface is divided into four segments. When the electric field is applied across one of the opposing electrode segments, the actuator will perform the bending deformation.

For practical applications, to increase the mechanical output, the actuators are usually driven at a high electric field. This takes the risk of failure and results in some deleterious effects, such as fracture and heat generation. Usually, several essential factors influence the failure and limit the performance of the piezoelectric actuators. These factors include electric field, temperature, stress, and frequency [24–36]. The effect of these factors on the behaviors of the piezoelectric bending type actuators operated at a high electric field were investigated and are summarized in this paper. The results are not only beneficial to the design and operation of the bending actuators, but also provide a good reference to the other types of piezo actuators or transducers.

Experimental

Both commercial and in-house fabricated actuators were applied in this work. The series and parallel bimorph were from Morgan Electro Ceramics (PXE5). The piezo tube came from the BPO Boston Piezo-Optics Inc. (Navy type III). The monomorph was in-house fabricated using EPD technique and the in-house synthesized materials PZT0 and PZT1 [20–23]. The properties of each material are listed in Table 1.

The performance of the bending actuator was measured using the setup as shown in Fig. 2. It consists of RT6000HVS ferroelectric tester (Radiant Technologies, Inc.), Vibraplane (RS Kinetic Systems, Inc.), MTI-2000 fotonic sensor (probe: MTI2032RX, MTI Instruments), FG3000 function generator (Yokogawa), PZD2000 high voltage amplifier (Trek), DL1640L oscilloscope (Yokogawa), IRI 1011 thermal imager (IRISYS), and HP4194A impedance analyzer. The samples were measured at clamped–free or free–free boundary conditions. The fotonic sensor was applied to measure the displacement, and the RT6000HVS ferroelectric tester was used for the polarization and static displacement measurement with a triangle signal at 2.5 Hz. In the dynamic measurement, the function generator, high voltage amplifier, and oscilloscope were used to measure the displacement, voltage, and current. The samples and experimental details are listed in Table 2.

Table 1 Material properties of the studied bending actuators

Materials	ρ (g/cm^3)	Q_m	tanδ	s_{11}^E (10^{-12}/Pa)	$\varepsilon_{33}^T/\varepsilon_0$	d_{31} (10^{-12} m/V)	Tensile strength (MPa)	T_c (°C)
PXE5	7.8	75	0.02	15	2100	−215	80	285
PZT1	7.6	–	–	11	688	−99.5	–	–
PZT0	7.4	–	–	18	719	−62.5	–	–
Navy type III	7.5	1000	0.004	10	1000	−97	75.8	300

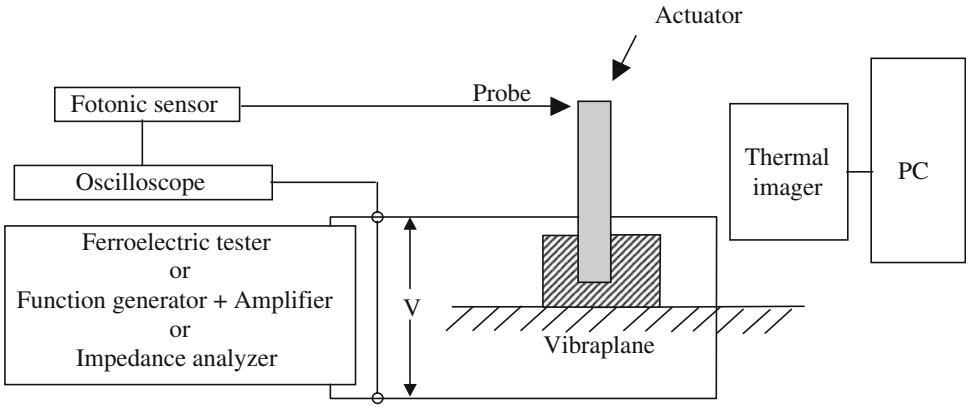

Fig. 2 Characterization setup of the bending actuators. Actuators were fixed on the vibraplane with different boundary conditions. Fotonic sensor was used to measure the displacement. Oscilloscope was used to record the readings of displacement, voltage, and current. Ferroelectric tester was used for polarization and static displacement measurement. Function generator and amplifier were used as power source of the actuator at dynamic state. Impedance analyzer was used to measure electric properties. Thermal imager was used to measure the temperature rise and distribution

Table 2 Experimental details of the studied bending actuators

Sections	Experimental cases	Actuator applied	Materials	Dimension (length-width-thickness mm^3)	Boundary condition	Parameters measured
3.2	Parallel even electric field actuator	Parallel bimorph	PXE5	11-6-0.6	Clamped–free	Displacement and polarization
3.3	Parallel uneven electric field actuator	Graded monomorph	PZT0 and PZT1	10.81-2.72-0.4	Clamped–free	Displacement and polarization
3.4	Antiparallel actuator	Series bimorph	PXE5	8-4-0.6	Clamped–free	Displacement and polarization
		Piezo tube	Navy type III	3.5-5-15 (inner diameter-outer diameter-length)	Clamped–free	Displacement and polarization
4.1	Vibration theory	Parallel bimorph	PXE5	11-6-0.6	Clamped–free	Displacement, admittance; theoretical frequency response of mechanical, electrical and thermal properties
4.2	Stresses	(a) Series bimorph	PXE5	8-4-0.6	Clamped–free	Displacement or velocity *vs.* frequency
		(b) Parallel bimorph		11-6-0.6	Clamped–free	
		(c) Series bimorph		35-1.6-0.6	Free–free	
4.3	Domain reorientation or depoling	(a) Series bimorph	PXE5	8-4-0.6	Clamped–free	Displacement, current, impedance, polarization
		(b) Parallel bimorph		11-6-0.6		
4.4	Heat generation and temperature rise	Graded monomorph	PZT0 and PZT1	10-2.6-0.26	Clamped–free	Displacement, temperature, electrical admittance, voltage and current
4.5	Frequency	Series bimorph	PXE5	69.98-1.6-0.62	Free–free	Temperature–stress–vibration velocity–frequency relations
				34.72-1.6-0.62		
				16.99-1.6-0.62		
				9.67-1.6-0.62		
				4.94-1.6-0.62		

Static situation

Superposition theory

Figure 3 shows the electric field induced polarization and displacement hysteresis curves of a piezoelectric plate made of material PXE5 at a frequency of 2.5 Hz. Initially, both displacement and polarization increase with the electric field. Above the coercive field, domain reorientation takes place and the displacement shows the typical butterfly shape. The saturated polarization P_s and remnant polarization P_r are 40 μC/cm^2 and 36 μC/cm^2, respectively, and the coercive field is about 1021 V/mm. The maximum displacement is noted to be >10 μm, corresponding to a strain of 0.1%. This behavior of displacement and polarization has been well known for a single piezoelectric material, which in essence reflects the nature of the material itself. However, when the piezo plate is made into a device, such as a bending actuator, the behavior may vary. In other words, it could also be affected by the configuration of the actuator.

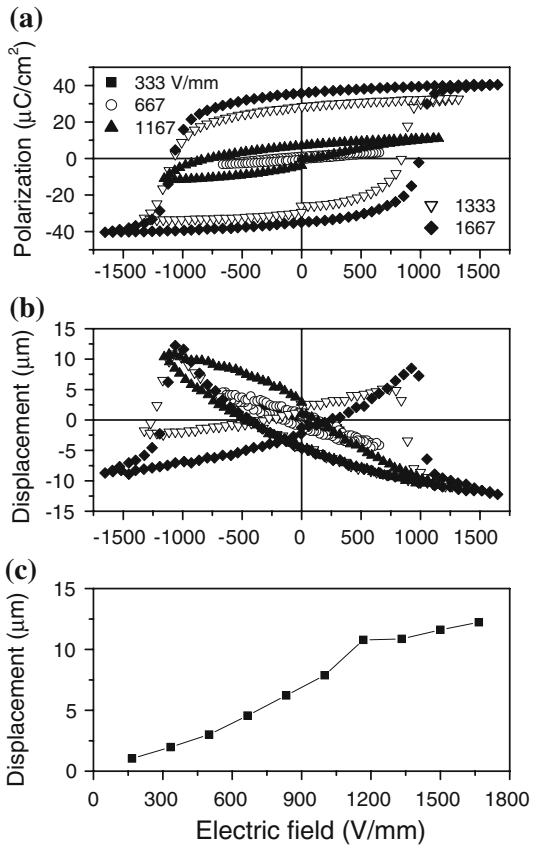

Fig. 3 Polarization and displacement of the piezo plate (PXE5, 11-6-0.6). **a** Polarization hysteresis loop. The saturated polarization P_s and remnant polarization P_r were 40 and 36 μC/cm^2, respectively, and coercive field was 1021 V/mm. **b** Displacement hysteresis loop. The magnitude of the loop increases with electric field. Above coercive field, the loop turned to the butterfly shape due to domain reorientation. **c** Magnitude of displacement versus electric field. It is a nonlinear relation. The maximum displacement was about 10 μm, corresponding to 0.1% strain

Taking bimorph as an example, the bending displacement can be expressed as [7]

$$\delta = \frac{d_{31} V l^2}{2/3 d^2} \tag{1}$$

where V is the applied voltage, l is the length, and d is the thickness. Rearranging the formula, it can be found that [37]

$$\delta = -\frac{3l}{8h}\left(d_{31}^{l} E_3^{l} l + d_{31}^{u} E_3^{u} l\right) = \frac{3l}{8h}\left(\delta^{u} + \delta^{l}\right) \tag{2}$$

$$\delta = -\frac{3 d_{31}^{l} E_3^{l} l^2}{8h} - \frac{3 d_{31}^{u} E_3^{u} l^2}{8h} = \delta^{U} + \delta^{L} \tag{3}$$

where the superscripts l or L and u or U represent the upper and lower layer of the bimorph actuator, $2h$ is the thickness, and E_3 is the electric field. It can be seen that the total displacement δ of the bimorph is the superposition of the upper layer plate longitudinal displacement δ^u at the unbonded free condition and the lower layer longitudinal displacement δ^l, multiplied by a constant geometrical factor $3l/8h$ (Eq. 2). It can also be regarded that the total displacement is the transverse displacement δ^U induced by the upper layer plate plus the transverse displacement δ^L induced by the lower layer plate (Eq. 3). In the later sections, this theory is used to explain the behaviors of the displacement hysteresis loop of various actuators by measuring the values of δ^u, δ^l, δ^U, δ^L.

Practically, according to the electric field and poling direction, the actuators as shown in Fig. 1 can be divided into three groups. The first is the parallel even electric field group, containing parallel bimorph and unimorph. In this group, the poling direction is parallel to the electric field and in each PZT layer, the electric field is evenly distributed. The second is the parallel uneven electric field group, including monomorph. In this group, the poling direction is parallel to the electric field. However, due to the difference of dielectric constant over the cross section of the actuator, the electric field is unevenly distributed. The third group is the antiparallel group, which contains series bimorph and piezo tube. In this group, the poling direction of one layer (or section of tube) is parallel, while the other layer is antiparallel, with the electric field.

Parallel even electric field actuator

Figure 4 shows the polarization and displacement hysteresis loop of the parallel bimorph. The coercive field was 1070 V/mm, which is close to the single plate sample. Because of the parallel application of the electric field, the saturated and remnant polarization (100 μm/cm^2 and

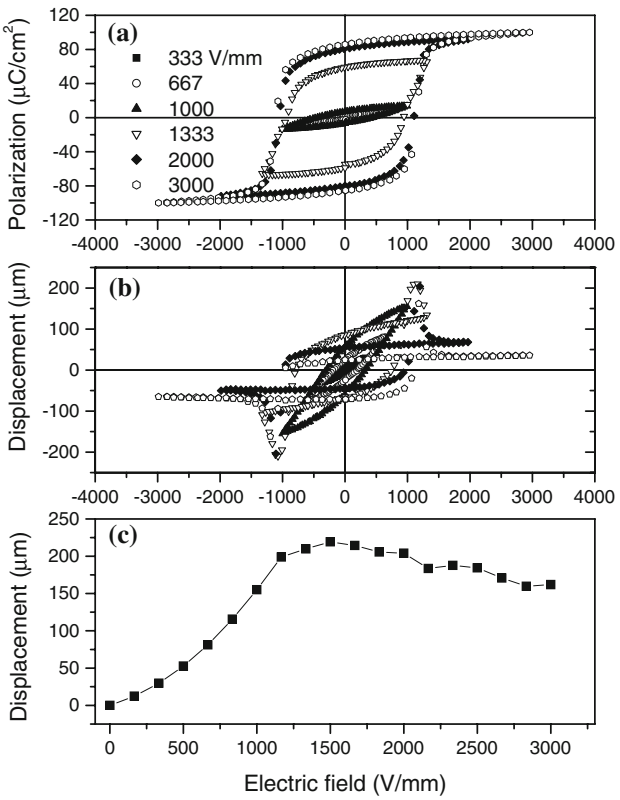

Fig. 4 Polarization and displacement of the parallel bimorph (PXE5, 11-6-0.6). **a** Polarization hysteresis loop. The saturated polarization P_s and remnant polarization P_r were 100 and 86 μC/cm^2, respectively, about twice that of the single plate in Fig. 3 due to the parallel configuration. **b** Displacement hysteresis loop. Above the coercive field, it showed the three-looped hysteresis curve instead of the butterfly shape. **c** Magnitude of displacement versus electric field. It shows nonlinear relation. Above coercive field, the magnitude tends to decrease

86 μm/cm^2, respectively) are about twice that of the single plate. For the displacement, it was interesting to find that a three-looped hysteresis curve, instead of the butterfly-shaped loop, was observed as shown in Figs. 4b and 5c when applied electric field exceeded the coercive field.

Figure 5a and b shows the measurement of the upper layer and lower layer induced displacements. It can be seen that the two butterfly shapes showed 180^o phase difference. Based on the superposition theory, the two displacement curves were superimposed in Fig. 5c, which gives exactly the same three-looped shape as that observed in Fig. 4b. This hence explains the formation of the three-looped hysteresis curve and also verifies the superposition theory. It is also noted that during the measurement of Fig. 5a and b, only one layer of PZT is active; hence the sample is essentially a unimorph, which gives the normal butterfly-shaped hysteresis loop. As a result, in the case of unimorph and parallel bimorph, it is confirmed that the individual active piezoelectric layer follows the behavior of a single piezoelectric material. However, the overall behavior of the actuator may look different, which is determined by the superposition of individual behavior.

Parallel uneven electric field actuator

In the case of monomorph, in the adjacent layer over the cross section, the dielectric constant will be different due to the different material compositions. According to Gauss's Law [37]

$$D_3 = E_3^i \varepsilon_{33}^{T^i} = E_3^{i+1} \varepsilon_{33}^{T^{i+1}} \quad (4)$$

The electric field therefore will be distributed based on the profile of dielectric constant over the cross section. As a result, upon application of the electric field, only areas where the actual field is above the coercive field will experience domain switching. Figure 6 shows the hysteresis loop of the polarization and displacement of a monomorph. A two-looped hysteresis displacement curve was observed, which

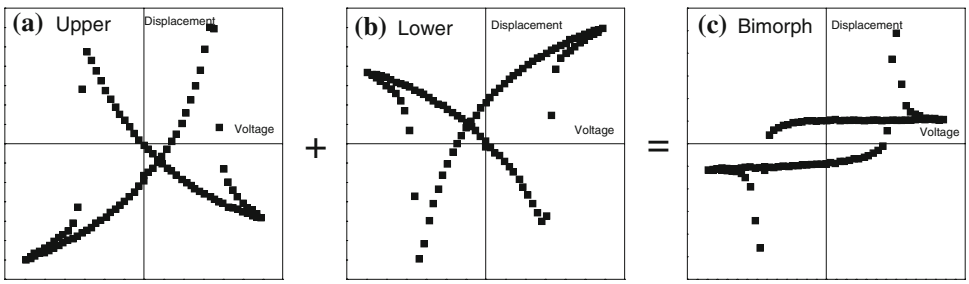

Fig. 5 Formation of the displacement hysteresis loop of the parallel bimorph. **a** Butterfly hysteresis loop induced by upper layer. Deactivating the lower layer but driving only the upper layer forms the butterfly shape. **b** Butterfly hysteresis loop induced by lower layer. Similar to **a**, driving only the lower layer forms the butterfly shape, however with a 180 degree phase difference with **a**. **c** Superposition of the two butterfly loops forms the three-looped hysteresis curve. This tells that the three-looped hysteresis curve is formed by superposition of the two out-of-phase butterfly loops

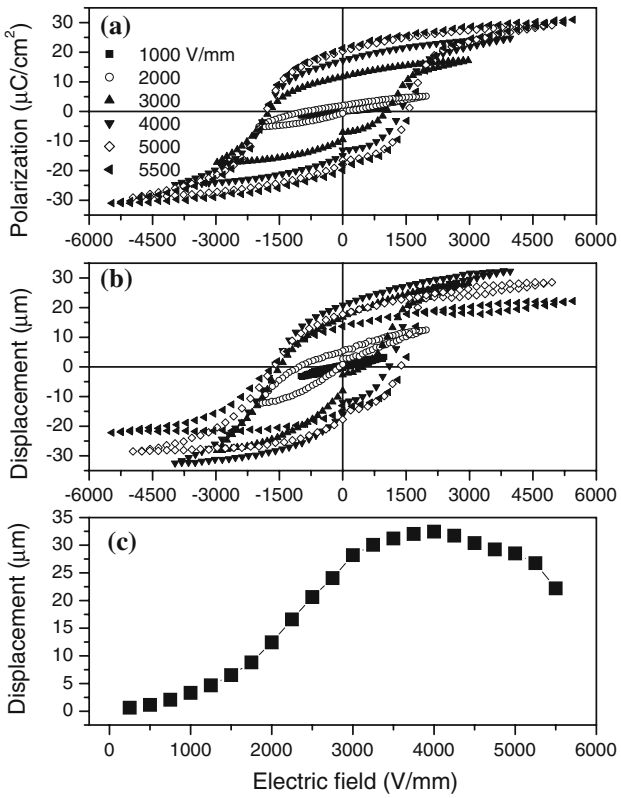

Fig. 6 Polarization and displacement hysteresis loop of the monomorph actuator (PZT0 + PZT1, 10.81-2.72-0.4). **a** Polarization hysteresis loop. Saturated and remnant polarization were 30 and 21 μC/cm^2, respectively, and coercive field was about 1600 V/mm. **b** Displacement hysteresis loop. A two-looped hysteresis curve is formed. **c** Magnitude of displacement versus electric field. It is a nonlinear relation. Above coercive field, displacement decreases

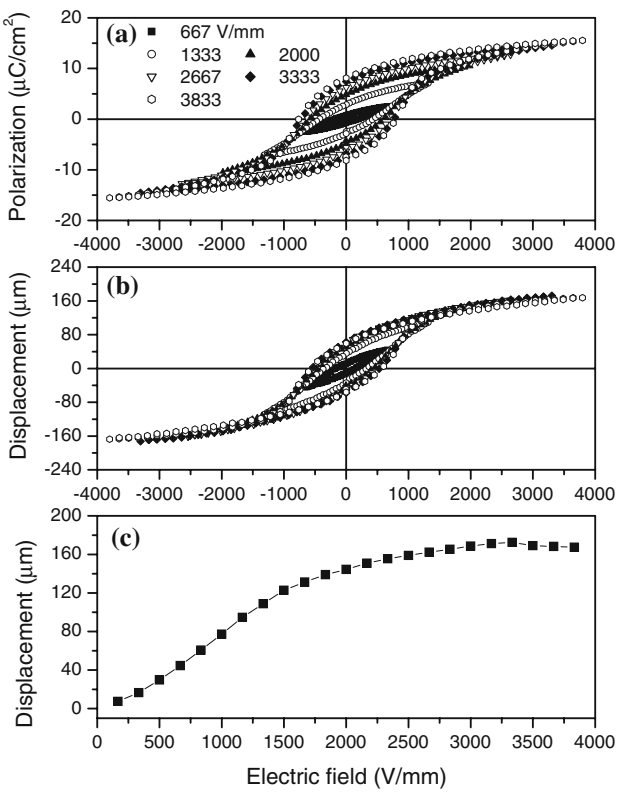

Fig. 8 Polarization and displacement hysteresis loops of the series bimorph (PXE5, 8-4-0.6). **a** Polarization hysteresis loop. Saturated and remnant polarization were 16 and 8 μC/cm^2, respectively, which are much lower than the plate sample in Fig. 3. **b** Displacement hysteresis loop. A one-looped hysteresis curved is formed. It is different from that of the single plate (Fig. 3) and parallel bimorph (Fig. 4). **c** Magnitude of displacement versus electric field. It is nonlinear and tends to saturate at the high electric field

is the superposition of a normal (without domain reorientation) and a butterfly-shaped (with domain reorientation) hysteresis loop as shown in Fig. 7.

Antiparallel actuator

Figure 8 shows the polarization and displacement curve of a series bimorph. It is very interesting that both saturated and remnant polarization (16 and 8 μC/cm^2, respectively) are much smaller than the plate sample. The butterfly-shaped displacement hysteresis loop was not observed until breakdown of the sample. This result indicates that the domain reorientation may be restricted in the series bimorph since larger magnitude of polarization will be produced during domain reorientation. Figure 9a and b shows the measured longitudinal displacement of the upper

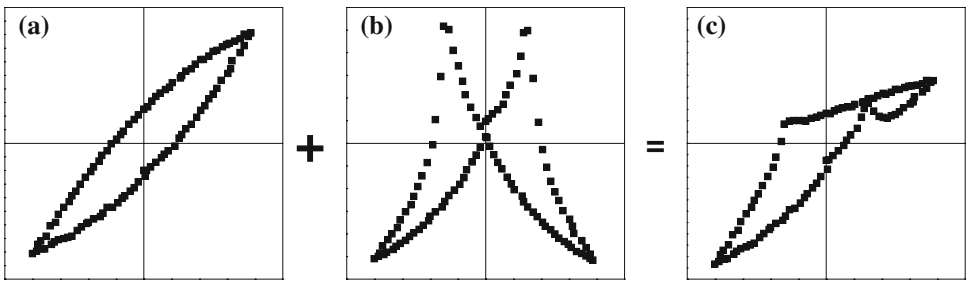

Fig. 7 Formation of the two-looped displacement hysteresis curve of the monomorph actuator. **a** Normal loop. Due to the graded nature of the actuator, portions where actual electric field is below the coercive field forms normal loop. **b** Butterfly loop. Portions above the coercive field form the butterfly shape. **c** Superposition of the two loop forms the two-looped hysteresis curve

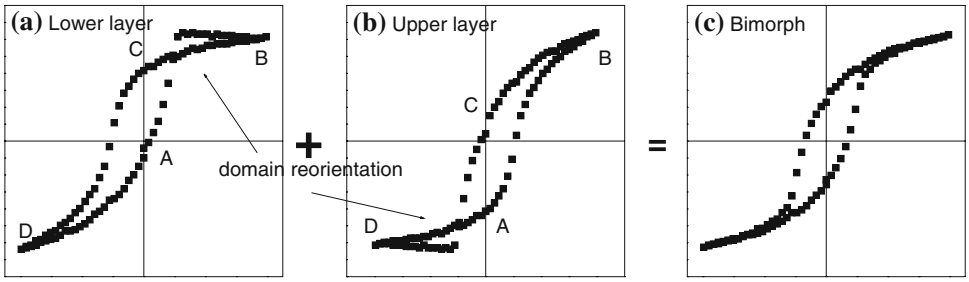

Fig. 9 Half butterfly hysteresis loop and superposition. **a** Longitudinal displacement of lower layer PZT. Portions of domain experience switching when electric field is antiparallel to the poling direction, inducing a half butterfly curve. **b** Longitudinal displacement of upper layer PZT. Similar to **a**, an out-of-phase half butterfly curve is formed. **c** Superposition of the two loops forms the one-looped hysteresis curve observed in Fig. 8

layer and lower layer PZT. It can be seen that only some regions of the domain experienced switching, which mainly were in poling direction–electric field antiparallel layer. This shows that the series bimorph is more resistant to the domain reorientation than the parallel bimorph. The behavior can be explained using the theory of "electric field redistribution" [37]. In the antiparallel layer, when the domain starts to switch, it will induce a large variation in dielectric constant. As a result, according to Gauss's Law (Eq. 4), the electric field in the antiparallel layer will decrease and become smaller than that in the parallel layer. This will prohibit the further reorientation of domains in the antiparallel layer. Therefore, the series bimorph is reckoned to be more stable and less apt to domain reorientation than the parallel bimorph. Figure 10 shows the result of the piezo tube. In contrast to the series and parallel bimorph which use the soft material PXE5, the piezo tube was made of a hard material Navy type III. However,

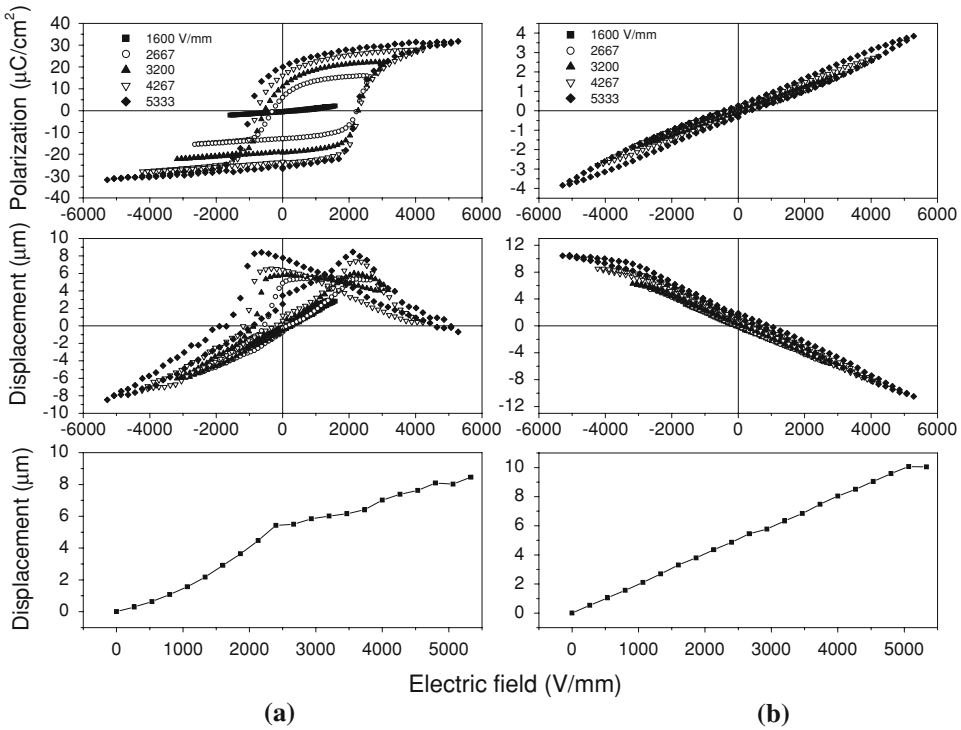

Fig. 10 Polarization and displacement hysteresis loops of the piezoelectric tube actuator (Navy type III, 3.5-5-15). **a** Polarization, displacement hysteresis loop, and magnitude of displacement versus electric field for longitudinal mode. The trends of polarization and displacement are similar to that of the plate sample in Fig. 3. **b** Polarization, displacement hysteresis loop, and magnitude of displacement versus electric field for bending mode. Even at a high electric field, the magnitude of polarization is small and displacement is linear. This is different from **a**, where above the electric field, butterfly-shaped displacement was observed. These results are consist with series bimorph (Fig. 8) and both cases prove that the actuator with antiparallel poling direction is more resistant to domain reorientation

similar results as that of the series bimorph were observed. Even at much higher electric field over the coercive field, the polarization and displacement of the bending actuator maintained linearity and small magnitude. In other words, no domain reorientation took place. This consistent result compared with the series bimorph proves that the antiparallel poling actuator is more resistant to domain reorientation. However it is to be noted that the hard material has larger coercive field. Therefore, it is expected that the hard material is able to withstand higher electric field. For example, the hard piezo tube maintained linearity up to 5333 V/mm (Fig. 10), while the soft series bimorph had shown significant nonlinearities below 3833 V/mm (Fig. 8).

$$I = \frac{2wh^3}{3} \tag{10}$$

where l is the effective length, w is the width, $2h$ is the thickness, ξ is the damping ratio, E_0 is the applied electric field, ω is the driving frequency, ω_1 is the first order natural frequency, ϕ is the phase lag, $Y(x)$ is mode shape, E is the Young's modulus, ρ is the density, I is the moment of inertia, A is the area of cross section, and λ and α are constants, which depend on the order of vibration. The variation of displacement as a function of frequency and mode shape is shown in Fig. 11a and b.

The mechanical stress of a bending actuator is [38]

$$T_1 = \left\{ \begin{array}{l} -\dfrac{1.174 \cdot \cos\phi \cdot d_{31}/s_{11}^E}{\sqrt{\left(1-(\omega/\omega_1)^2\right)^2+4\xi^2(\omega/\omega_1)^2}}(\cosh\lambda x+\cos\lambda x+\alpha(\sinh\lambda x+\sin\lambda x))+\dfrac{d_{31}}{s_{11}^E} \\ \quad +i\dfrac{1.174 \cdot \sin\phi \cdot d_{31}/s_{11}^E}{\sqrt{\left(1-(\omega/\omega_1)^2\right)^2+4\xi^2(\omega/\omega_1)^2}}(\cosh\lambda x+\cos\lambda x+\alpha(\sinh\lambda x+\sin\lambda x)) \end{array} \right\} E_0 e^{(i\omega t)} \tag{11}$$

Dynamic situation

Vibration theory

Mechanical properties

Displacement, vibration velocity, and mechanical stress are three of the important considerations for the application of a bending actuator. According to Euler–Benoulli beam theory, the displacement $u(x,t,\omega)$ of a vibrating bimorph cantilever can be expressed as [38]

$$u(x,t,\omega) = \frac{0.334 \cdot l^2/h \cdot d_{31} \cdot Y(x)}{\sqrt{\left(1-(\omega/\omega_1)^2\right)^2+4\xi^2(\omega/\omega_1)^2}} E_0 e^{i(\omega t-\phi)} \tag{5}$$

$$\tan(\phi) = \frac{2\xi\omega_1\omega}{\omega_1^2-\omega^2} \tag{6}$$

$$Y(x) = \cosh\lambda x - \cos\lambda x + \alpha(\sinh\lambda x - \sin\lambda x) \tag{7}$$

$$\omega_1 = \lambda^2\sqrt{\frac{EI}{\rho A}} \tag{8}$$

$$\left\{ \begin{array}{l} \lambda l = 1.875104 \\ \alpha = -0.734096 \end{array} \right. \tag{9}$$

Its magnitude decreases along the length of the actuator as shown in Fig. 11c. The peak stress (maximum stress $T_{1\max}$) arises at the clamped end. The relationship between the vibration displacement amplitude (u_0) and the velocity amplitude (v_0) at the vibration tip is given by the expression [38, 39]

$$v_0 = \omega u_0 = \varphi\frac{T_{1\max}}{\sqrt{E\rho}} \tag{12}$$

In this equation, φ is called the "shape factor" [39–41], which depends on the vibration mode and boundary condition of the actuator. For a bimorph with clamped–free boundary condition, the shape factor is calculated to be 0.58, and for free–free boundary condition, it is calculated to be 0.73. For a longitudinal vibration uniform rod, the shape factor is 1.0 [39–41]. If a displacement amplification horn is used, the shape factor can also be improved to be larger than one [39–41]. Eq. 12 has indicated the following essential features: (1) The maximum achievable vibration velocity relies on the peak stress of the actuator, which needs to be lower than the tensile strength of the materials [38, 39, 42]. (2) The maximum achievable displacement will decrease when frequency increases since the maximum velocity is a constant. (3) Increasing the shape factor improves the vibration velocity.

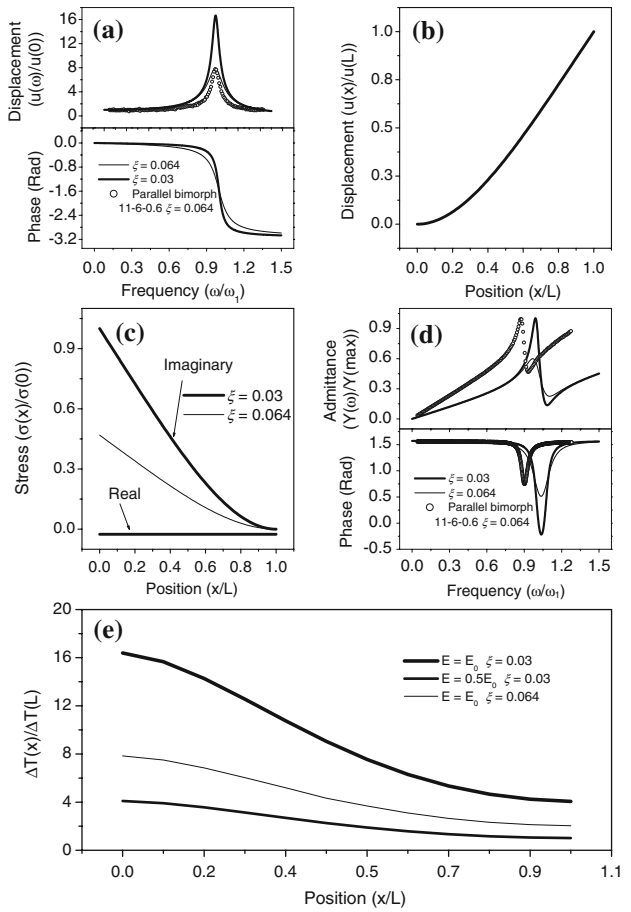

Fig. 11 Theoretical prediction of the responses of the piezoelectric bending actuators under clamped–free boundary condition. **a** Displacement versus frequency. Displacement reaches maximum at the resonant frequency. The lower damping ratio ξ produces higher resonant displacement. **b** First order bending vibration mode shape under clamped–free boundary condition. The curvature of the clamped cantilever reduces from the clamped to the free end. **c** Stress distribution along the length of the actuator. The maximum stress is at the clamped end. The lower damping ratio produces higher stress due to the higher vibration amplitude. **d** Admittance versus frequency. The maximum admittance is observed at the resonant frequency, and lower damping ratio results in higher magnitude of admittance. **e** Temperature distribution along the length of the actuator. With higher electric field and lower damping ratio, the actuator gives higher vibration amplitude but with more electrical loss and stress magnitude. This results in the higher temperature rise. The maximum temperature is at the clamped end of the actuator

Electrical properties

The electrical admittance of the cantilever is [38]

$$Y = G + iB = -\omega \frac{0.920 \cdot k_{31}^2 \varepsilon_{33}^T \cdot \sin\phi \cdot wl/2h}{\sqrt{\left(1-(\omega/\omega_1)^2\right)^2 + 4\xi^2(\omega/\omega_1)^2}} - i\omega \left\{ \frac{0.920 \cdot k_{31}^2 \varepsilon_{33}^T \cdot \cos\phi \cdot wl/2h}{\sqrt{\left(1-(\omega/\omega_1)^2\right)^2 + 4\xi^2(\omega/\omega_1)^2}} + \varepsilon_{33}^T \left(1-k_{31}^2\right)\frac{wl}{2h} \right\} \quad (13)$$

Figure 11d shows the variation of admittance as a function of frequency and the phase lag between current and voltage.

Thermal properties

The temperature rise of an actuator is determined by the heat generation and dissipation. The heat generation is due to the losses of the materials. The loss power is expressed as [38, 39]

$$Q_{\text{gen}} = Q_{\text{mec}} + Q_{\text{ele}} \quad (14)$$

$$Q_{\text{mec}} = \frac{1}{2}\omega s_{11}^E T_1^2 \tan\delta_{\text{m}} \quad (15)$$

$$Q_{\text{ele}} = \frac{1}{2}E_{\text{o}}^2 \omega \varepsilon_{33}^T \tan\delta_{\text{e}} \quad (16)$$

where Q_{mec} and Q_{ele} are the mechanical and electrical loss per unit volume, which are proportional to the square of stress T_1 and electric field E_0, respectively. In Eqs. 15 and 16, $\tan\delta_e$ is the dielectric loss and $\tan\delta_{\text{m}}$ (=$1/Q_{\text{m}} = 1/(2\xi)$) is the mechanical loss tangent [43, 44]. Here Q_{m} is the mechanical quality factor and ξ is the damping ratio. Q_{m} is an important parameter that not only affects the loss of the materials, but also determines the magnitude of vibration displacement, velocity, stress, and admittance [38, 39]. For high power actuator or transducer applications, a high Q_{m} is necessary [38, 39].

Since the mechanical loss depends on the stress, the temperature must vary along the length of the actuator because the stress magnitude is different at each point of the length as shown in Fig. 11c. The following equation describes the "temperature mode shape" of the actuator [38]

$$\begin{aligned}\Delta T = {} & C_1 e^{\sqrt{A_c h'/Ak}x} + C_2 e^{-\sqrt{A_c h'/Ak}x} \\ & + \frac{F(1+\alpha)^2}{-16Ak\lambda^2 + 4A_c h'} e^{2\lambda x} + \frac{F(1-\alpha)^2}{-16Ak\lambda^2 + 4A_c h'} e^{-2\lambda x} \\ & + \left(\frac{F(1+\alpha)\left(-\alpha A_c h' + 2Ak\lambda^2\right)}{-4A^2k^2\lambda^4 - A_c^2 h'^2} \right) e^{\lambda x} \sin\lambda x \\ & + \frac{F(1+\alpha)\left(-A_c h' + 2\alpha Ak\lambda^2\right)}{-4A^2k^2\lambda^4 - A_c^2 h'^2} e^{\lambda x} \cos\lambda x\end{aligned}$$

$$+\frac{F(1-\alpha)\left(-A_c h' + 2\alpha A k\lambda^2\right)}{-4A^2k^2\lambda^4 - A_c^2 h'^2} e^{-\lambda x}\cos\lambda x$$
$$+\frac{F(1-\alpha)\left(-\alpha A_c h' + 2A k\lambda^2\right)}{-4A^2k^2\lambda^4 - A_c^2 h'^2} e^{-\lambda x}\sin\lambda x$$
$$+\frac{F(1-\alpha^2)}{8Ak\lambda^2 + 2A_c h'}\cos 2\lambda x$$
$$+\frac{\alpha F}{4Ak\lambda^2 + A_c h'}\sin 2\lambda x + \frac{J}{A_c h'} \quad (17)$$

where A is the area of cross section, A_c is the perimeter of the vibrating actuator, k is the thermal conductivity, h' is the heat transfer coefficient, and the rest are listed below:

$$\begin{cases} A_1 = \sqrt{\frac{A_c h'}{Ak}} + \frac{h'}{k} & A_2 = \left(-\sqrt{\frac{A_c h'}{Ak}}\right) + \frac{h'}{k} \\ A_3 = \left(-\frac{h'}{k}\Delta T0\right) - d\Delta T0 & A_4 = \sqrt{\frac{A_c h'}{Ak}} e^{\sqrt{\frac{A_c h'}{Ak}}l} + e^{\sqrt{\frac{A_c h'}{Ak}}l}\left(\frac{h'}{k}\right) \\ A_5 = \left(-\sqrt{\frac{A_c h'}{Ak}}\right) e^{-\sqrt{\frac{A_c h'}{Ak}}l} + e^{-\sqrt{\frac{A_c h'}{Ak}}l}\left(\frac{h'}{k}\right) & A_6 = \Delta Tl\left(-\frac{h'}{k}\right) - d\Delta Tl \\ C_1 = \frac{A_2A_6 - A_3A_5}{A_2A_4 - A_1A_5} & C_2 = \frac{A_3A_4 - A_1A_6}{A_2A_4 - A_1A_5} \\ C: \text{ Stress constant} & D = E_0 d_{31}/s_{11}^E \\ E = \frac{1}{2}AE_o^2\omega\varepsilon\tan\delta & B = \frac{1}{2}A\omega s_{11}^E \tan\delta_m \\ F = BC^2 & J = F + BD^2 + E \end{cases}$$

Numerical solutions of the above equations are shown in Fig. 11e. The maximum temperature rise happens at the clamped end, which is consistent with the position of the maximum stress.

Stresses

Stresses can result in fracture of the sample. Figure 12a and b shows the velocity of both series and parallel bimorphs as a function of frequency and electric field. It can be seen that for both bimorph, at the low electric field, the actuator shows a velocity peak at the mechanical resonant frequency, which increases in magnitude, and shifts to lower frequency end as electric field increases. When approaching a certain degree, the continuity of the curve is broken and the velocity drops suddenly. On further increase of the electric field, this phenomenon, however, disappears (more elaboration and discussion in the next section).

Figure 13 reveals that the break in the curve is due to the fracture of the sample. As analyzed earlier, the mechanical limitation of the vibration velocity is imposed by the tensile strength of the materials [38, 39, 42]. As driving field increases, both velocity and stress increase accordingly. When reaching the tensile strength limitation, fractures occur at the peak stress location, which is the clamped end for a cantilever configuration as analyzed earlier. For free–free vibration bimorph, the peak stress occurs at the center. As a result, the sample will fracture at the center as shown in Figs. 12c and 13c.

Domain reorientation or depoling

After the fracture, the phenomenon however disappears despite further increase in the electric field as shown in Fig. 12. This is because the failure mechanism has changed from the fracture to domain reorientation or depoling [38, 39, 42]. Therefore, the velocity is not observed to reach that of the fracture level, but decreases very soon once domain reorientation takes place, as illustrated in Fig. 12a and b.

An indication of domain reorientation is the distortion and magnitude increase of the current profile as shown in Fig. 14. The current profile deviates from the original sinusoidal wave, and a sharp peak is observed. This is attributed to the domain orientation, which induces large polarization variation within a short time. As a result, the current abruptly changes according to the following relation [38, 42]

$$I = \frac{\mathrm{d}Q}{\mathrm{d}t} = A\frac{\mathrm{d}D}{\mathrm{d}t} \approx A\frac{\mathrm{d}P}{\mathrm{d}t} \quad (18)$$

Domain reorientation can also be revealed from the experiment, where the impedance of the parallel bimorph was measured after high voltage frequency scan using the parallel or series connections, as shown in Fig. 15. In the original sample, the poling direction of the upper layer and lower layer is parallel. The vibration resonance and anti-resonance peaks can be observed clearly in Fig. 15a–d.

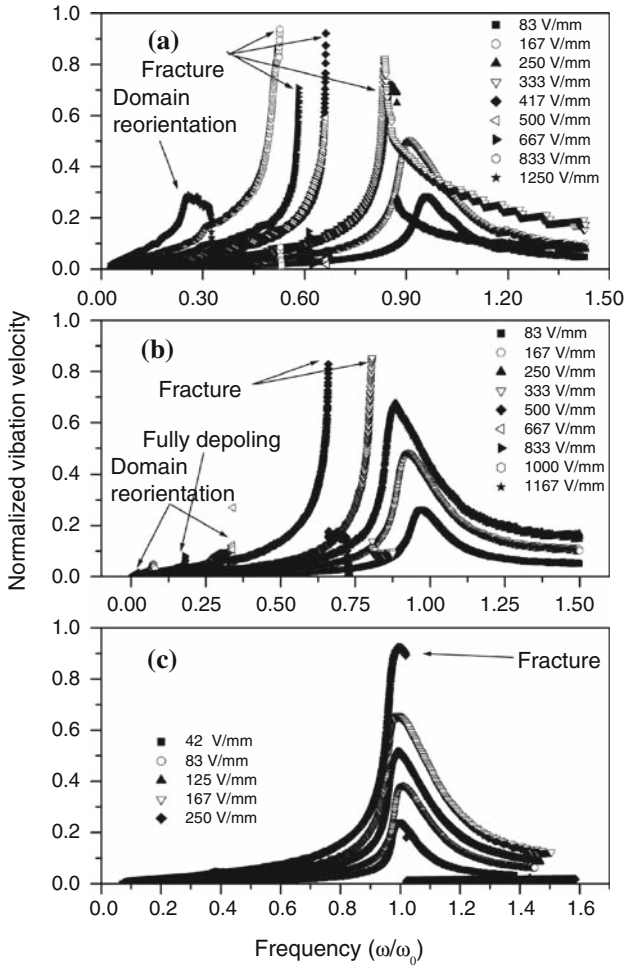

Fig. 12 High electric field responses of piezoelectric bending actuators. **a** Velocity versus frequency of series bimorph under clamped–free boundary condition. Before 833 V/mm, the failure mode was fracture, which was indicated by the sudden drop of the velocity during frequency scan. The maximum velocity is limited by the tensile strength of the materials. Above 833 V/mm, the failure mode was domain reorientation or depoling. The maximum velocity also decreases when domain reorientation takes place. **b** Velocity versus frequency of parallel bimorph under clamped–free boundary condition. The trend is similar with series bimorph in **a**. However, below 500 V/mm, the failure mode was fracture. Above it, the failure mode was domain reorientation or depoling. Compared with series bimorph, it is less resistant to domain reorientation since lower electric field is required to trigger domain reorientation. **c** Velocity versus frequency of series bimorph under free–free boundary condition. Within the applied electric field range, the failure mode was fracture

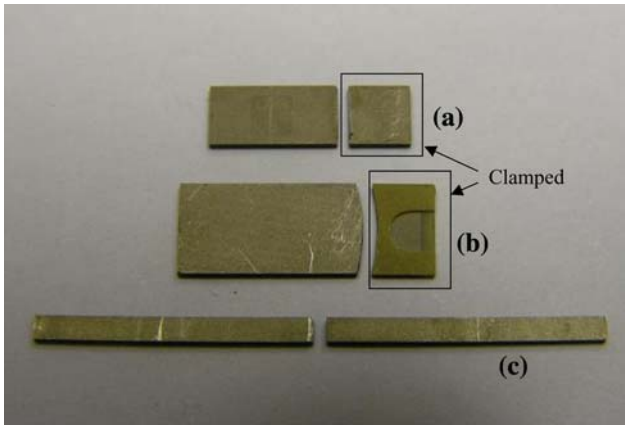

Fig. 13 Fracture of piezoelectric bending actuators. **a** Series bimorph under clamped–free boundary condition. Fracture took place at the clamped end due to the maximum stress at that location. **b** Parallel bimorph under clamped–free boundary condition. Fracture took place at the clamped end due to the maximum stress at that location. **c** Series bimorph under free–free boundary condition. In contrast to **a** and **b**, fracture took place at the center of the actuator because the maximum stress arises there under this boundary condition

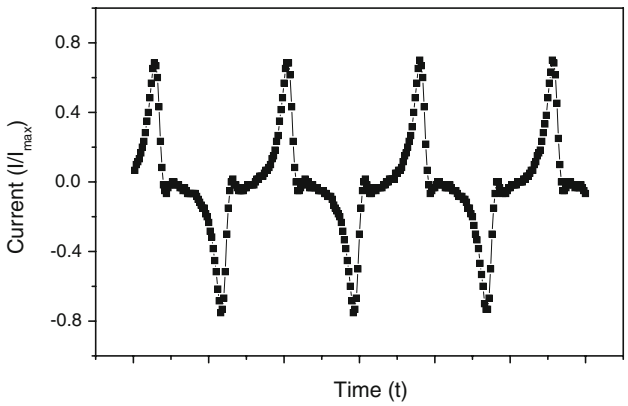

Fig. 14 Distortion of the current profile over time. The current is no longer sinusoidal after domain reorientation

However, if domain reorientation takes place, the poling direction of the upper and lower layer will turn to the antiparallel direction as shown in Fig. 15f and g. Hence, with the parallel connection (Fig. 15f), the vibration peak will not be observed as the vibration has turned to the longitudinal mode. Nevertheless, using the series connection (Fig. 15g), the vibration mode will still be bending; hence vibration peak remains. The results shown in Fig. 15a–d in general agree with the above analysis, except for the case of Fig. 15b, where the expected vibration peaks in both connections were not observed, suggesting a complete depoling of the sample.

On comparing the series and parallel bimorph, domain reorientation was observed to take place at the electric field above 500 V/mm for parallel bimorph, while above 800 V/mm for series bimorph in the dynamic state. This indicates that the series bimorph has higher resistance to the domain reorientation, which is consistent with the static observations. However, even at the electric field value of 800 V/mm, it is still lower than the static coercive field of the materials, which is about 1000 V/mm. One of the main reasons for this will be the heat generation, which will be explained in the next section.

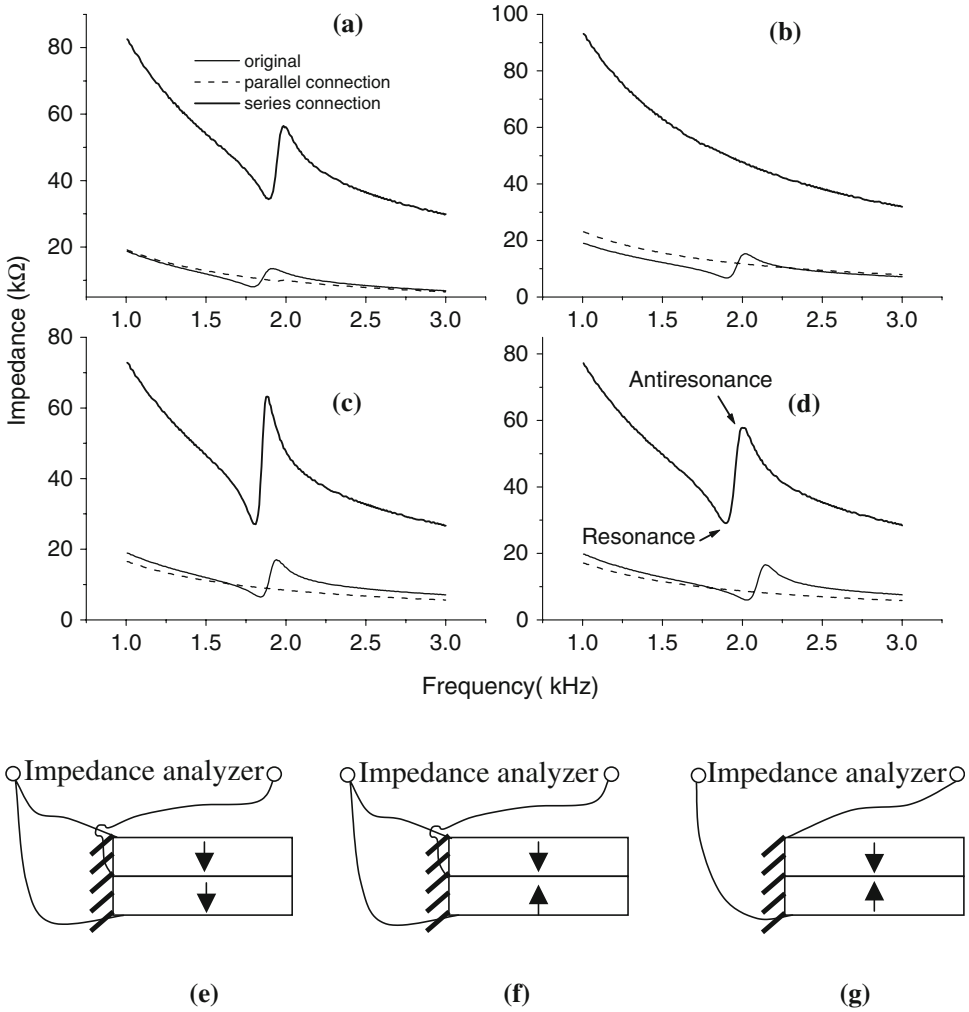

Fig. 15 Impedance spectrum of the parallel bimorph (PXE5, 11-6-0.6) before and after high voltage frequency scan. **a** Comparison of impedance curve after 400 Vp-p high voltage scan. The poling direction has been changed from parallel (**e**) to antiparallel (**f** or **g**). Therefore only using the series connection, the bending mode indicated by the resonant peak can be observed. Using the parallel connection, the longitudinal mode can be excited. But it is out of the frequency range studied. Therefore no peak was observed. **b** Comparison of impedance curve after 500 Vp-p scan. No peaks were observed. Therefore depoling took place fully. **c** Comparison of impedance curve after 600 Vp-p scan. The result is same as **a**. **d** Comparison of impedance curve after 700 Vp-p scan. The result is same as **a**. **e** Poling direction and connection of original sample. **f** Poling direction and parallel connection of tested sample. **g** Poling direction and series connection of tested sample

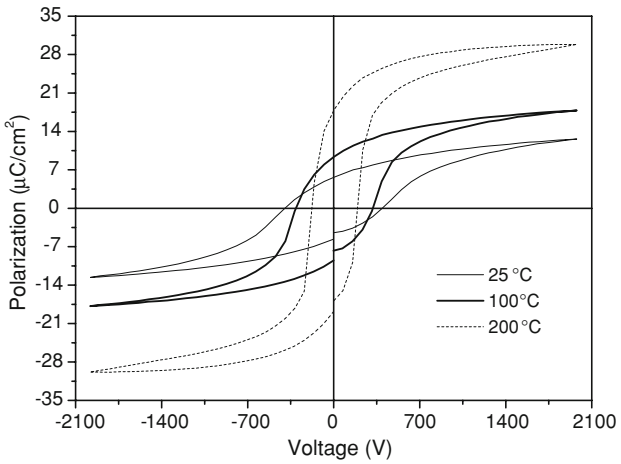

Fig. 16 Polarization hysteresis loop of series bimorph (PXE5, 8-4-0.6) as a function of temperature. As temperature rises, the coercive field decreases. This eases the domain reorientation, which is indicated from the increased magnitude of the polarization

Heat generation and temperature rise

As discussed earlier, heat generation and temperature rise resulted from the mechanical and electrical losses of the materials. As temperature increases, the coercive field of the materials will decrease as shown in Fig. 16 [42, 45]. As a result, it eases the domain reorientation. Figure 17 shows a high field frequency scan of a monomorph actuator, where domain reorientation accompanied with high temperature rise was observed. Because of the internal friction, domain reorientation will produce a large amount of heat, which in turn accelerates the reorientation process. This, in turn, results in abrupt increase in current and temperature, which can be observed from Fig. 17b and c. Figure 18 shows the observed temperature mode shape of the monomorph. It can be seen that high temperature was observed at the clamped end of the actuator, which is consistent with the theoretical analysis.

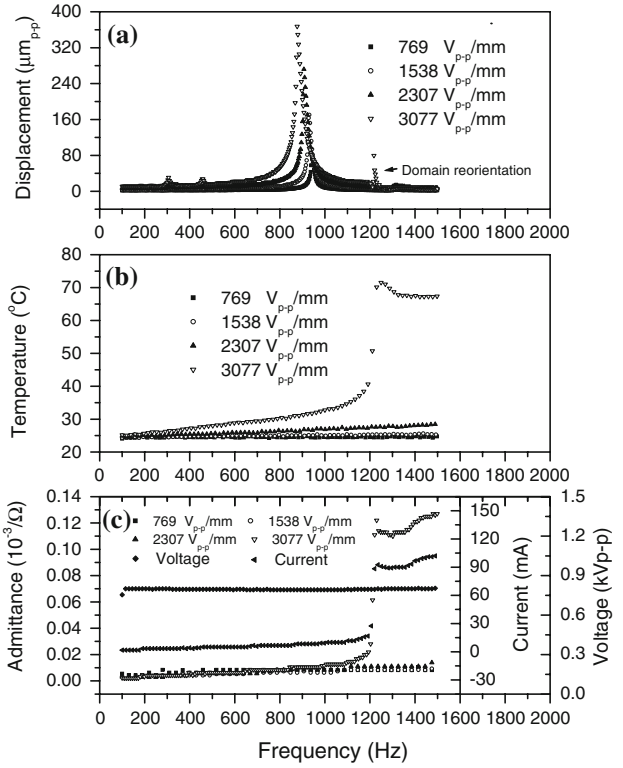

Fig. 17 Frequency and electric field response of monomorph actuator (PZT0 + PZT1, 10-2.60-0.26). **a** Displacement versus frequency as a function of electric field. Domain reorientation is indicated by the irregular peak in the figure, and distorted current profile was observed. **b** Temperature versus frequency as a function of electric field. Upon domain reorientation, a large amount of heat was produced and a sudden increase of temperature was observed, which in turn accelerates the domain reorientation. **c** Admittance, current, and voltage versus frequency as a function of electric field. Upon domain reorientation, an abrupt increase of current and admittance was also observed

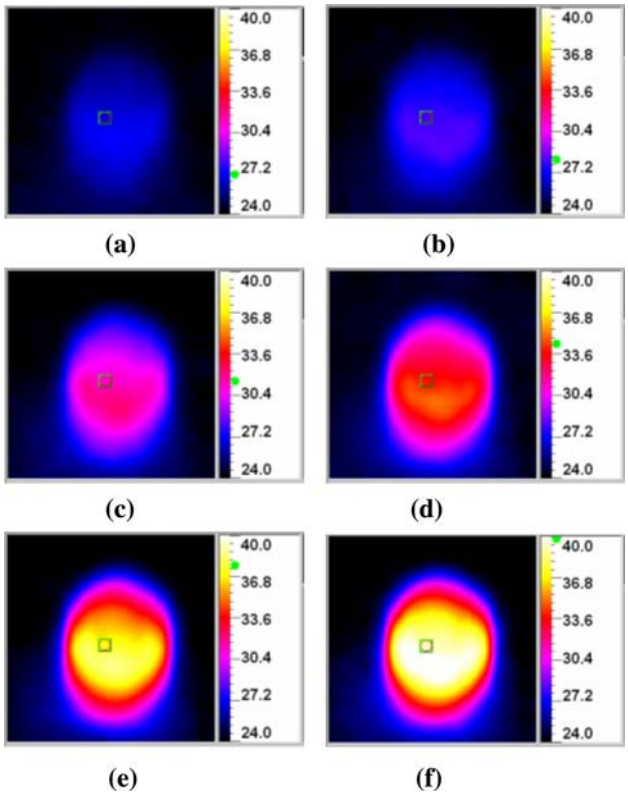

Fig. 18 Temperature distribution of monomorph (PXE5, 10-2.60-0.26) at **a** 408 Hz. **b** 522 Hz. **c** 879 Hz. **d** 1090 Hz. **e** 1163 Hz. **f** 1188 Hz. The high temperature was observed at the clamped end of the actuator, which is the location of maximum stress

Frequency

As shown in Eqs. 15 and 16, both electric loss and mechanical loss are proportional to the frequency, which will affect the performance of the actuator accordingly. Figure 19a gives the 3D relation between stress, temperature, electric field, and frequency. Figure 19b–d shows the projections of Fig. 19a in Temperature rise–Electric field, Temperature rise–Stress, and Electric field–Stress planes. The stress was calculated from the velocity using Eq. 12. From Fig. 19, it can be deduced that in general when the resonant frequency is low (0.39 kHz, 1.55 kHz and 6.56 kHz), the actuator is able to vibrate at a high amplitude, approaching its mechanical limitation with a low temperature rise even though the electric field is high. The failure mode was observed to be the fracture. However, when the frequency is high (19.88 kHz, 75.45 kHz), the actuator produces a lot of heat. Temperature rise becomes significant compared with that of the low frequency actuator. As a result, the velocity cannot be maintained at a high vibration level and decreases significantly. Comparing the impedance curve before and after the test (Fig. 20), it is noted that there exists a difference in the magnitude of impedance, which indicates the different domain states before and after test since the parameters such as k_{31}, ε_{33}^{T}, which constitute the impedance (1/admittance) as shown in Eq. 13, depend on the domain states of the materials. Therefore the failure modes are reckoned to be the domain reorientation or depoling caused by the losses and heat generation during the high voltage frequency scan operations.

It should also be noted that in the earlier studies on vibration velocity, mainly the loss mechanism was considered, which gives the velocity limitation at about 1 m/s [24–36, 46–51]. In fact, it is more appropriate to suggest that the vibration velocity is frequency dependent. At low frequency, it mainly depends on the tensile or fatigue strength (for long-term application) of the materials. On the other hand, as frequency increases, the losses will become the dominating mechanism, which results in the reduction of the vibration velocity. This is also consistent with the results shown in Fig. 19, where the 0.39 kHz actuator

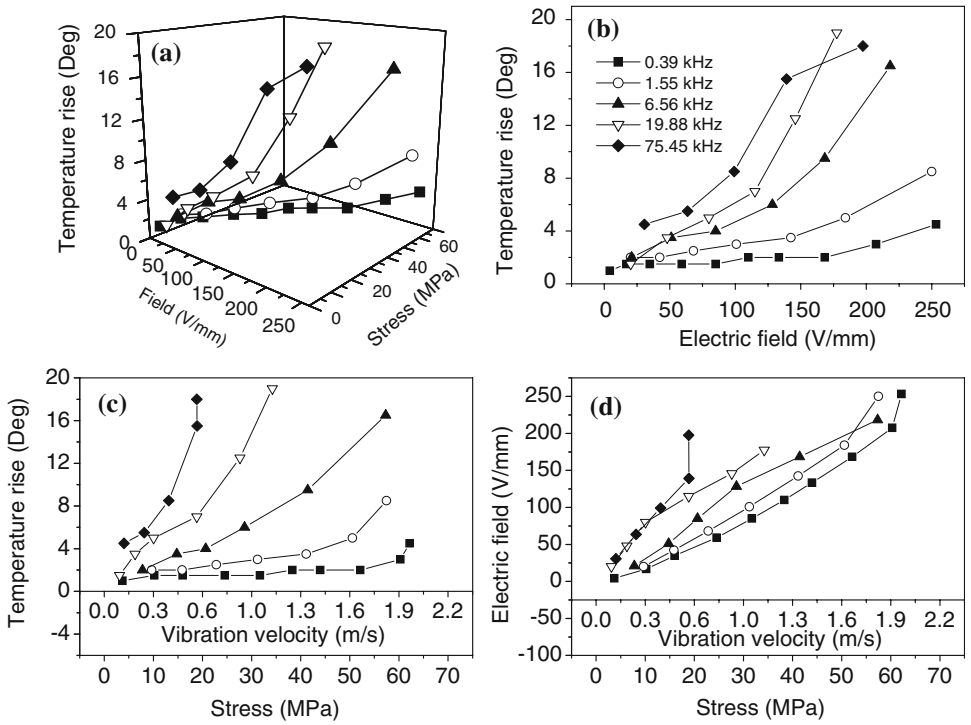

Fig. 19 Relation of velocity, stress, electric field, temperature, and frequency. **a** Temperature versus electric field versus stress as a function of frequency. Generally, high frequency actuators produced more losses and achieved lower vibration velocity. **b** Temperature versus electric field as a function of frequency. As electric field increased, the temperature increased accordingly. The higher frequency actuator produced more heat than the low frequency actuator at the same electric field level. **c** Temperature versus velocity (stress) as a function of frequency. The lower frequency actuators achieved larger vibration velocity with lower heat generation than the high frequency actuator. **d** Electric field versus velocity (stress) as a function of frequency. To achieve the same vibration velocity, high frequency actuator needs higher electric field

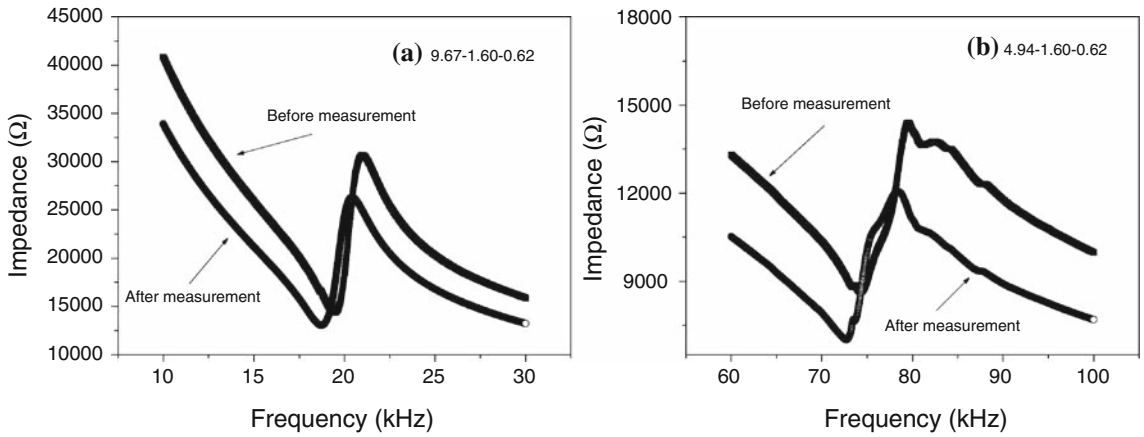

Fig. 20 Comparison of impedance before and after velocity measurement. **a** 19.88 kHz actuator. **b** 75.45 kHz actuator. The impedance curves do not coincide before and after test, indicating the change of material properties. This is caused by domain reorientation or depoling

reached a vibration velocity of about 2 m/s, but the 75.45 kHz transducer only achieved 0.6 m/s.

Since at low frequencies the vibration velocity is limited by mechanical properties of the materials, the performance of soft and hard materials will not be significantly different. This can be revealed from Eq. 12 and Table 1 (PXE5 and Navy type III) as they have similar density, compliance, and strength. Hence, at the low frequency range, soft material is also a good choice for high vibration amplitude applications. However, at the high frequency range, the results will be different. Because the loss mechanism dominates and hard materials have lower mechanical loss

(high Q_m) and electrical loss (low tanδ) as shown in Table 1, hard materials will be better than soft materials in terms of vibration velocity, heat generation, stability, and application frequency range. Hard materials also have a larger coercive field, which makes them more resistant to depoling and domain reorientation. Therefore at the high frequency range, hard materials will be superior to soft materials. As a result, hard materials are generally used for high power application, such as ultrasonic motor and sonar transducer.

Conclusions

It is shown that the performance of piezoelectric actuator depends on several important factors including electric field, stress, temperature rise, and frequency. The parameters are also noted to be interlinked and coupled with each other. In the static situation, domain reorientation and breakdown voltage limit the maximum displacement of the actuator. The displacement and polarization hysteresis loop are affected by the electric field and poling direction. At antiparallel configuration, electric field redistribution takes place, which prohibits the domain reorientation. This effect makes the series bimorph more stable and resistant to domain reorientation than the parallel bimorph. The dynamic condition is found to be much more complicated. As the stress is usually high due to the high vibration amplitude, the strength of the materials becomes the theoretical mechanical limitation of vibration velocity, especially at the low frequency range. However, when the frequency is high, the velocity will decrease due to the increase of electrical and mechanical losses indicated by the heat generation and temperature rise. Therefore, effective heat dissipation is essential for high electric field, high stress, and high frequency operations of the piezoelectric actuators.

References

1. Uchino K (2004) In: Proceedings of the international conference on smart materials-smart/intelligent materials and nanotechnology, p 67
2. Wiederick HD, Sherrit S, Mukherjee BK (1989) In: Second workshop on military robotic applications, p 214
3. APC International Ltd. (2001) Piezoelectric ceramics: principles and applications. APC International, Ltd, Mackeyville, PA
4. Damjanovic D (1998) Rep Prog Phys 61:1267
5. Safari A (1999) Mater Res Innovat 2:263
6. Taylor CJ, Washington GN (2002) In: Smart structures and materials 2002: smart structures and integrated systems. Proceedings of SPIE 4701 2002, p 443
7. Uchino K (1997) Piezoelectric actuators and ultrasonic motors. Kluwer Academic Publisher, London
8. Niezrechi C, Brei D, Msokalik A (2001) Shock Vib Dig 33: 269–280
9. Haertling GH (1999) J Am Cram Soc 82:797
10. Moulson AJ, Herbert JM (2003) Electroceramics. John Wiley & Sons Ltd, England
11. Smits JG, Dalke SI, Cooney TK (1991) Sens Actuator A 28:41
12. Besell M, Johansson S (1999) J Electroceram 3:73
13. Yoo JH, Hong JI, Cao WW (2000) Sens Actuator A 79:8
14. Yeo CY, Shim WK, Wouterson E, Li T, Ma J (2008) Funct Mater Lett 1:225
15. Chen YH, Li T, Ma J, Boey FYC (2007) Key Eng Mater 334–335:1077
16. Li T, Chen YH, Ma J (2005) J Mater Sci 40:3601. doi: 10.1007/s10853-005-0643-6
17. Li T, Chen YH, Ma J, Boey FYC (2007) Key Eng Mater 334–335:1073
18. Li T, Ma J, Chen YH (2004) Ceram Int 30:1803
19. Li T, Ma J, Chen YH (2005) Ferroelectrics 315:111
20. Chen YH, Ma J, Li T (2004) Ceram Int 30:1807
21. Chen YH, Li T, Ma J (2003) J Mater Sci 38:2803. doi: 10.1023/A:1024468015242
22. Chen YH, Li T, Ma J (2006) J Mater Sci 41:8079. doi: 10.1007/s10853-006-0015-x
23. Chen YH, Ma J, Li T (2004) Ceram Int 30:683
24. Kanda T, Kobayashi Y, Higuchi T (2003) Jpn J Appl Phys 42:3014
25. Umeda M, Nakamura K, Ueha S (1999) Jpn J Appl Phys 38:5581
26. Tashiro S, Ikehiro M, Igarashi H (1997) Jpn J Appl Phys 36:3004
27. Chen WP, Chong CP, Chan HLW, Liu PCK (2003) Mater Sci Eng B99:203
28. Xu CH, Hu JH, Chan HLW (2002) Ultrasonics 39:735
29. Calderon-Moreno JM, Popa M (2002) Mater Sci Eng A336:124
30. Fett T, Munz D, Thun G (2000) J Mater Sci Lett 19:1921
31. Uchino K, Zheng J, Yoshikawa S (1998) J Electroceram 2:33
32. Takahashi S, Sasaki Y, Uchino K (1995) Jpn J Appl Phys 34:5328
33. Uchino K, Hirose S (2001) IEEE T Ultrason Ferr 48:307
34. Takashi S, Hirose S, Uchino K (1994) J Am Ceram Soc 77:2429
35. Wang QM, Zhang QM, Cross LE (1999) J Appl Phys 86:3352
36. Sasaki Y, Umeda M, Inoue T (2001) Jpn J Appl Phys 40:5743
37. Li T, Chen YH, Boey FYC, Ma J (2007) Sens Actuator A 134:544
38. Li T, Chen YH, Boey FYC, Ma J (2007) J Electroceram 18:231
39. Li T, Chen YH, Ma J (2007) Sens Actuator A 138:404
40. Eisner E, Seager JS (1965) Ultrasonics 88-98
41. Lin ZM (1987) Ultrasonic horn principle and design. Science press, Beijing, China (in Chinese)
42. Li T, Chen YH, Ma J (2009) Mechatronics 19:520. doi: 10.1016/j.mechatronics.2008.12.003
43. Silva CWD (2000) Vibration: fundamentals and practice. CRC Press, London
44. He LX, Li CE, Liu W (2000) Phys Stat Sol A 179:275
45. Setter N, Colla EL (1993) Ferroelectric ceramics, tutorial reviews, theory, processing, and applications. Birkhauser verlag, Basel Boston Berlin
46. Takashshi S, Hirose S (1993) Jpn J Appl Phys 32:2422
47. Hirose S, Aoyagi M, Tomikawa Y (1993) Jpn J Appl Phys 32:2418
48. Yamamoto T, Mizuno F (1995) Jpn J Appl Phys 34:2627
49. Takahashi S, Sasaki Y, Hirose S (1997) Jpn J Appl Phys 36:3010
50. Umeda M, Nakamura K, Ueha S (1998) Jpn J Appl Phys 37:5322
51. Takahashi S, Yamamoto M, Sasaki Y (1998) Jpn J Appl Phys 37:5292